# Simulation Design and Testing of a Dielectric Embedded Tapered Slot UWB Antenna for Breast Cancer Detection

**Dheyaa T. Al-Zuhairi[1, *], John M. Gahl[2], Adil Al-Azzawi[2], and Naz E. Islam[2]**

**Abstract**—A distortion-less ultra-wideband tapered slot antenna is designed to achieve wide band impedance matching and high gain without requiring coupling liquids. The antenna is embedded in a suitable dielectric material for compact size and performance improvement. The near-field test is simulated by placing several field probes near the antenna to plot the radiation pattern and polarization isolation. The antenna exhibits a highly directive pattern and polarization isolation in near field. The time domain antenna distortion is tested by calculating the fidelity and group delay. The results show low distortion and also show the importance of covering the antenna by dielectric layers for bandwidth increment and distortion reduction. To evaluate the antenna performance in breast cancer detection, three breast phantoms are imaged by using the raster scan imaging method. Two approaches are proposed to detect tumors without the need of breast background data. The approaches based on the effect of the tumor on transmission and reflection parameters on the frequency band allowed for medical applications. The obtained images show the antenna to be a strong candidate for breast imaging as well as in tumor detection for different scenarios that include complex multi-layer phantom and small tumor.

## 1. INTRODUCTION

In 2002, the Federal Communications Commission (FCC) allocated the 3.1 to 10.6 GHz frequency range for ultra-wideband (UWB) research and applications [1]. The technology of UWB offers important advantages, including low power consumption and a large bandwidth. An important application UWB technology is breast cancer detection through imaging [2, 3]. Breast cancer is a very dangerous and deadly disease and an early detection of smaller tumors have a better chance of successful treatment [4]. Because of their wide bandwidth and high gain, tapered slot antennas (TSAs) have been utilized in breast cancer detection [5, 6].

Several ideas in improving UWB TSA have been proposed over the years for different applications. New geometrical gratings were proposed to improve the radiation pattern and antenna gain, reduce side lobes, and sharpen beam width at low frequency [7]. Some of these attempts were for a TSA enclosed in a dielectric rod for gain improvement in communications and radar systems [8]. For microwave breast cancer detection systems, a balanced antipodal Vivaldi antenna was designed with a profiled higher dielectric constant material to increase the antenna directivity [9]. Another wide band compact microstrip-fed TSA was proposed with corrugations to reduce size and improve gain [10]. Here the antenna was covered by dielectric layers to protect it from the coupling liquid. In 2013, another antipodal Vivaldi antenna was proposed to improve the radiation patterns and gain at higher frequencies, where the lens and the choke slot edges configuration were loaded at the termination of the flares [11]. Chen et al. [12] proposed a broadband artificial material that acted as a lens for beam focusing and was

* Corresponding author: Dheyaa T. Al-Zuhairi (dtaqq3@mail.missouri.edu).
[1] Currently with Electrical and Computer Engineering, University of Missouri Columbia, USA and is also associated with College of Engineering-University of Diyala, Iraq. [2] Electrical and Computer Engineering, University of Missouri Columbia, USA.

composed of non-resonant parallel-line unit cells to improve the gain of an antipodal TSA. Another modification was introduced by drilling corrugations on the edges of metallic flaring section and placing periodic metallic strips on the slot area on the Vivaldi antenna to improve the gain especially at low frequencies of the coverage band [13].

There are many methods and techniques for imaging microwave. Aperture raster scan is a microwave imaging method used in biomedical applications. It is a simple and fast image acquisition method, where water was used initially as a coupling liquid between the antenna and tissue [14], but at the cost of supplementary loss, complicated system maintenance and limited resolution [15]. The need for coupling liquid can be eliminated with antenna size reduction using aperture raster scan [15, 16]. However, such a scanning method is a two steps process; first it requires a scan of the breast phantom with tumors absent, which is the background for farther imaging, and secondly one needs to subtract the background from the image when the tumors are present. This approach of course cannot work clinically because there is no background information for the breast to be tested. Moreover, the antennas in such cases are relatively large, and the obtained images need to be post-processed by blind de-convolution algorithm to obtain de-blurred images.

In order to fix the issues mentioned in the previous paragraph, we propose a high gain UWB-TSA for microwave breast imaging. The antenna is embedded between two layers of dielectric material to increase the gain and delivered power. By covering the antenna with dielectric layers, the need for coupling liquid for impedance matching has been eliminated. An industry standard simulation suite (CST microwave studio) has been used in this work to design and analyze the antenna. The antenna performance in breast cancer detection was tested using aperture raster scanning method. Two approaches are introduced to detect tumors without requiring background information.

With this brief introduction, we divide the rest of the paper as follows. In Section 2, we discuss the design and dimensions of the antenna, adding corrugations and matcher. Here we also discuss the reasons for using the specific dielectric layers. Section 3 shows the numerical and simulated antenna performance and tests results, including the effects of corrugations and dielectric slabs. In Section 4, the effects of tumor on the $S$-parameters are shown. The imaging setup using a 2D raster scan method, image acquisition approaches, and resulting images are presented in Section 5. We present our conclusions in Section 6.

## 2. ANTENNA DESIGN

The proposed antenna is a modified form of the regular exponentially tapered slot antenna (TSA). The geometry of our proposed antenna is shown in Fig. 1(a). The design consists of five parts, which include the radiator, ground plane, main substrate layer and two additional layers of dielectric (one over the metal and the second below the main substrate). The main substrate layer and the extra dielectric layers are Rogers RT6010 with a relative dielectric constant $\varepsilon_r = 10.2$ with thickness mentioned in the
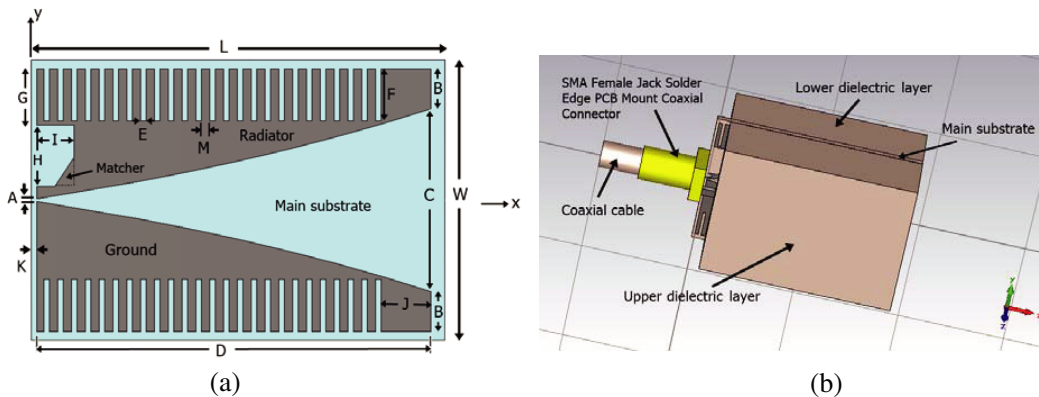


**Figure 1.** (a) Geometry of the designed antenna without the upper and lower dielectric. (b) 3-D of the whole antenna.

next paragraph. The exponential slot of the antenna is defined through the following equation [12]:

$$y = c_1 e^{Rx} + c_2 \qquad (1)$$

where $R$ is a parameter that controls the shape of the exponential curve of the antenna, and $c_1$ and $c_1$ are constants that can be calculated from Eqs. (2) and (3) below, where point $(x_1, y_1)$ is the feed point, and $(x_2, y_2)$ is the end of the antenna,. The ground plate is the lower metallic part of the antenna as shown in Fig. 1(a).

$$c_1 = \frac{(y_2 - y_1)}{e^{(Rx_2)} - e^{(Rx_1)}} \qquad (2)$$

$$c_2 = \frac{y_1 e^{(Rx_2)} - y_2 e^{(Rx_1)}}{e^{(Rx_2)} - e^{(Rx_1)}} \qquad (3)$$

For simulation, the antenna is printed first on a 1 mm thickness main substrate of Rogers RT6010 with dimensions of $W = 26\,\text{mm} \times L = 38.5\,\text{mm}$ as depicted in Fig. 1(a). A 9 mm thick dielectric layer of this material is also placed under the main (1 mm) substrate and finally a 10 mm layer of the same material is placed over the metal to give the final shape shown in Fig. 1(b). The thickness of the dielectric slabs is chosen such that the antenna final size is still acceptable and minimize signal distortion. The use of the dielectric layers of $\varepsilon_r = 10.2$ provides: i) an impedance matching over an ultra-wide band of frequency, ii) a high gain and, iii) a compact antenna without the need of coupling liquids. Using coupling liquids results in additional losses and complicates the conservation and sterilization of a clinical setting [15].

The space between the radiator and the ground plate at the feeding point, parameter A, and parameter B in Fig. 1(a), are optimized through the simulation software to get as low reflection coefficient as possible. Table 1 shows the antenna parameters. A space of 0.5 mm (parameter $K$ in Fig. 1(a)) is left to ensure that the ground is separated from the coaxial connector and only connected by a small soldering region. The antenna is fed by a $50\,\Omega$ coaxial cable and a SMA connector is used to connect the antenna to the coaxial cable. RG142 coaxial cable is simulated to feed the antenna. The corrugations or etched slots on the radiator and ground of the antenna are added to improve the performance as discussed in Subsection 2.1.

**Table 1.** Proposed antenna's parameters.

| Parameter | A | B | C | D | E | F | G | H | I | J | K | L | M | W |
|-----------|------|------|-------|----|-----|------|-----|-----|-----|------|-----|------|-----|----|
| Length (mm) | 0.24 | 3.72 | 16.96 | 37 | 0.5 | 4.85 | 5.2 | 5.7 | 3.5 | 4.65 | 0.5 | 38.5 | 0.8 | 26 |

The parameter $R$ plays an important role in determining the general performance of the antenna that include the bandwidth, return losses, gain and signal distortion. After generating a set of $R$ values, such as 0.5, 0.3, 0.1, 0.08, 0.06, 0.04, 0.02 and 0.01, we found that $R = 0.02$ is the optimal parameter for our design. As the electric field develops between the radiator and the ground plate inside the exponential opening, it then propagates vertically from the tapered end to the breast tissues. Thus, the antenna has a vertically polarized signal.

## 2.1. Adding Corrugations to the Antenna

Corrugations are used to improve the performance parameters of an antenna and extend the frequency band toward low frequencies [7, 14, 17, 18]. Here the length of the slots must be less than a quarter-wavelength at the lowest operating frequency, which is 3.1 GHz [18]. Fig. 2(a). shows the effect of the corrugations on the VSWR for the proposed antenna. It is obvious that the slots not only increase the antenna frequency band by decreasing VSWR below 2 at low frequencies but also reduce the VSWR for all of the band of the frequencies between 3.1GHz to 10.6 GHz.

The dimensions of the designed antenna's slots are given as E, F, and M in Table 1 for the width, length, and space between two adjacent slots, respectively. Figs. 2(b) and 2(c) show the surface current without and with corrugations cases at the central frequency (6.85 GHz), respectively. The current distribution between the radiator and the ground is asymmetric without the slits. Corrugations direct

(a)                                                                          (b)                                                                          (c)
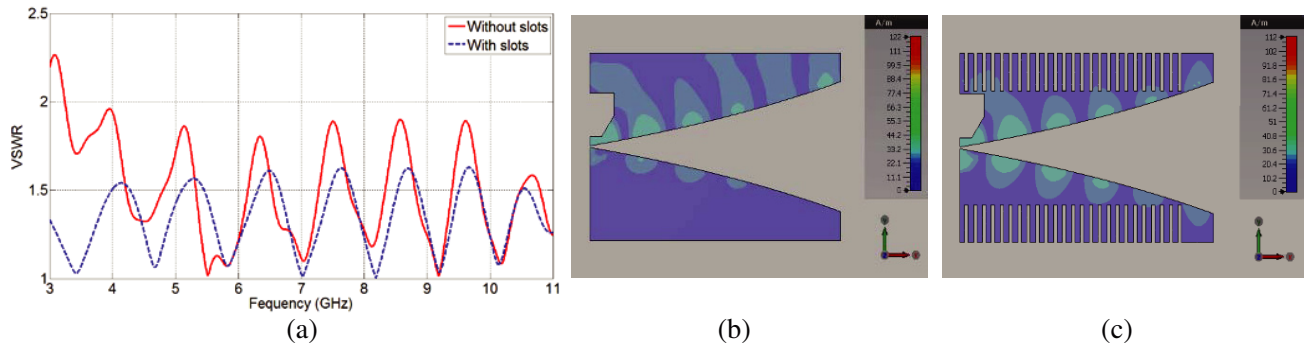
**Figure 2.** (a) VSWR in absence and present of corrugations. (b) Surface current flow on the antenna at 6.85 GHz without corrugations. (c) Surface current flow on the antenna at 6.85 GHz with corrugations.

surface current to distribute along the exponentially open edges and minimize current flow through the slits at the top and bottom of the antenna as shown in Fig. 2(c). Thus, with adding of slots, the gain is improved, and radiation is maximized in the horizontal $(x)$ axis.

## 2.2. The Antenna Matcher

The triangular segment shown in Fig. 1(a) functions as an impedance matcher between the antenna and the $50\,\Omega$ coaxial cable. By changing the dimensions of this triangle, the $S_{1,1}$ parameter can be tuned. The best match occurs when the triangle is described by the following three vertices (1.7 mm, 1.3 mm), (3.5 mm, 1.3 mm), and (3.5 mm, 4 mm) in the $X, Y$ plane.

## 2.3. Dielectric Material Layers

As stated earlier, covering the radiator and ground of the antenna by layers of a dielectric material improves impedance matching as also discussed in Section 3.1. For the proposed antenna, however, it is important to mention that the two layers of the dielectric (upper and lower) do not cover the entire length of the antenna. The upper and lower dielectrics start 2 mm from the feed point of the antenna to allow for soldering and radiation pattern symmetry. Using these layers adds gain on all frequency components in the band, and consequently increases the power delivered to the breast and reduces the power radiated in the free space around the antenna.

The raster scan imaging method, which is used in this work, depends on the directivity and the beam width of the antenna. The more directivity and the narrower beam width antenna has, the better breast imaging can be obtained. In addition to the aforementioned advantages of the dielectric material layers, it is found that these layers can control the time domain dispersion of the transmitted signal, as discussed in detail in Section 3.

## 3. SIMULATION AND ANALYSIS

The antenna has been simulated and tested after optimizing its parameters, as described in Section 2. The tests and analysis include impedance matching, gain, near-field radiation pattern, polarization and distortion.

## 3.1. Reflection Coefficient and Gain Analysis

The antenna performance was analysed in the frequency domain for return loss and gain. The return loss was tested without and with the dielectric layers, in order to show the importance of the dielectric layers in matching the antenna without using any coupling liquid. As shown in Fig. 3, the impedance matching is improved over the entire frequency band by embedding the antenna in the dielectric material. After using the dielectric slabs and for a return loss of $-10\,$dB, the designed antenna operating frequency
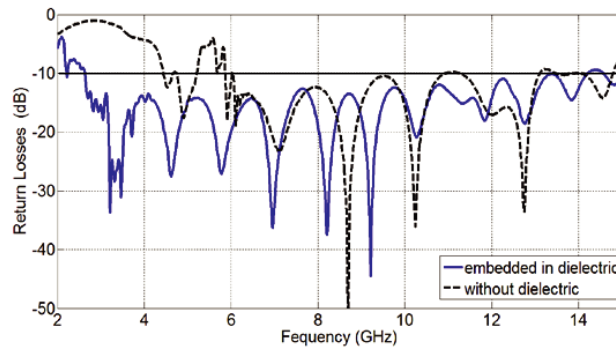
**Figure 3.** Return loss of the designed antenna with and without dielectric slabs.
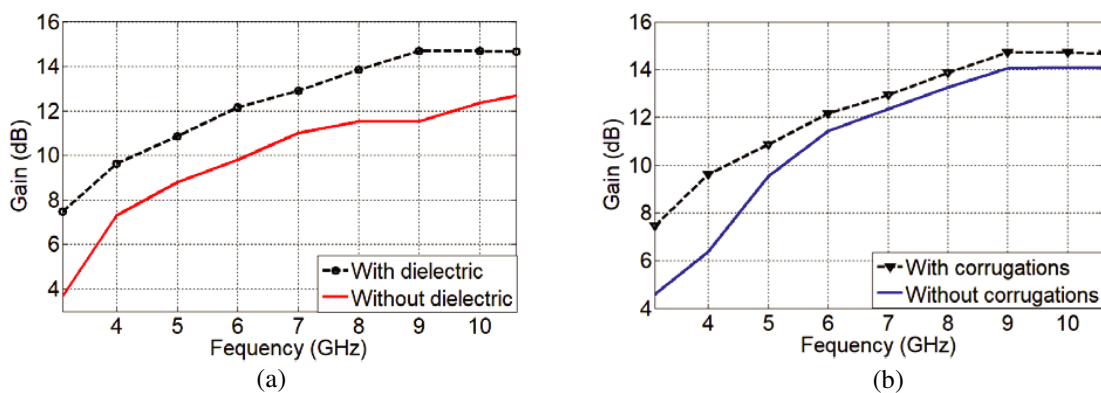


**Figure 4.** (a) Gain of the antenna with and without dielectric slabs in the band of interest. (b) Gain of the antenna with and without corrugations in the band of interest.

band is from 2.63 GHz to 14.2 GHz. The gain of the antenna is evaluated over the FCC band (3.1 GHz–10.6 GHz) while considering two factors that include adding; i) dielectric slabs and, ii) corrugations as described earlier. Fig. 4(a) shows the gain of the antenna with and without the dielectric slabs but with etched corrugations for both cases, while Fig. 4(b) shows the effect of corrugations on the gain in the presence of dielectric slabs. It is evident from the figures, the dielectric layers improve the gain by around 2.4 dB in average, over the entire band. Using corrugations enhances the gain in all frequency band, especially at the low frequencies. In conclusion, the final antenna design, after utilizing dielectric slabs and corrugations, has high gain even at low frequencies with a minimum value of 7.47 dB and a maximum of 14.7 dB.

## 3.2. Near-Field Radiation Pattern and Polarization

The antenna is designed for imaging with direct contact with the breast, and thus needs to be tested in the near field. To test the antenna, several $E$-field probes are distributed in the near field on a plane perpendicular to the boresight line ($y$-$z$ plane) at 10 mm from the front of the antenna in $x$-direction. The antenna centre point is located along $x$ at $y = 0$ mm and $z = 0$ mm. The probes are distributed along the $E$-plane and $H$-plane in steps of 5 mm from $y = -25$ mm to $y = 25$ mm and $z = -25$ mm to $z = 25$ mm as shown in Fig. 5. At each of these locations, a pair of probes is used, one to measure vertical polarization electric field and the other to record the horizontal polarization component of the electric field. The purpose of this test is to test the antenna directivity and polarization isolation in near-field region.

The test includes three frequencies which are 4 GHz, 7 GHz, and 9 GHz. The electric field recorded at each probe, $E$, is used to calculate average power density or the time-average Poynting vector which
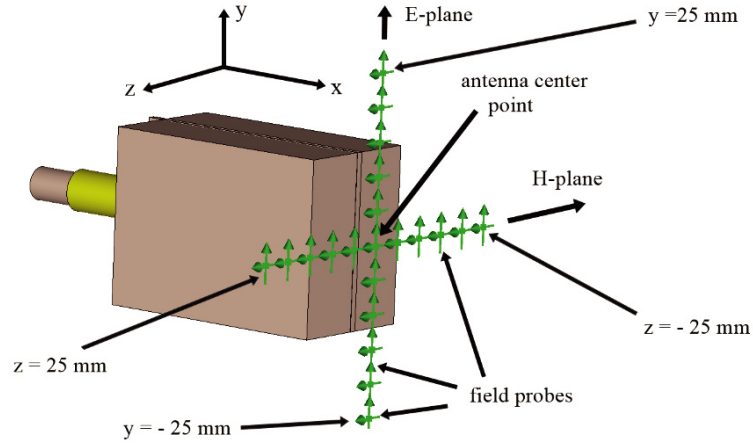
**Figure 5.** Near-field test configuration.



(a)                                    (b)                                    (c)
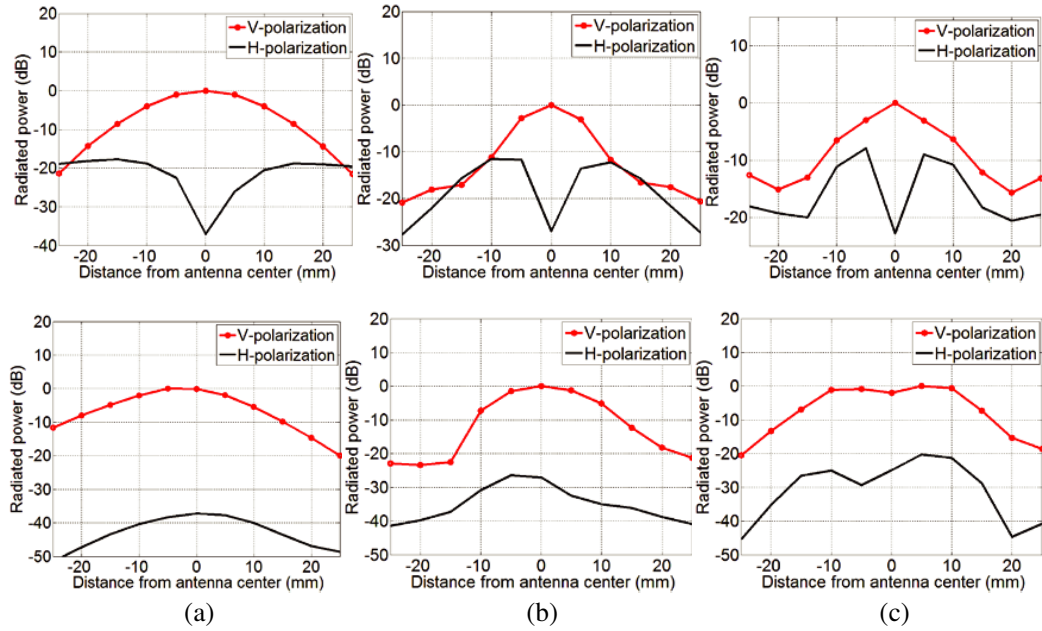
**Figure 6.** Near-field directivity and polarization isolation at (a) 4 GHz, (b) 7 GHz and (c) 9 GHz. $E$-plane in bottom and $H$-plane in top.

can be found as:

$$S_{av} = \frac{1}{2}\text{Re}\left[E \times H^*\right] \text{ or } S_{av} = \frac{|E|^2}{2\eta_o} \tag{4}$$

where $\eta_o = \sqrt{\frac{\mu_o}{\varepsilon_o}}$ is the intrinsic impedance of free space. To obtain the average power radiated by the antenna at 10 mm, the average power density is integrated over a square plane of 50 mm aside. This plane area covers all the probe locations. The radiated power is normalized and plotted to show the antenna radiation pattern and polarization isolation in near-field region.

The antenna radiated powers in the $E$-plane and $H$-plane are shown in Fig. 6. From this figure, it is clear that the radiated power in the near field is concentrated within $\pm 10$ mm of the antenna center point. As will be discussed later in Section 5, this narrow pattern will help in tumor detection with an accurate location as possible in the raster scan method. Fig. 6 also shows the polarization isolation

between the two linear polarization components of the electric field. At the main beam direction or antenna centre point, which is the point of interest in raster scan imaging method, the polarization isolation is almost 37 dB, 27 dB and 23 dB for 4 GHz, 7 GHz, and 9 GHz, respectively for both $E$-plane and $H$-plane. This demonstrates our earlier contention that the antenna is vertically polarized.

## 3.3. Fidelity and Signal Distortion

To calculate the antenna fidelity [19], two identical designs of the antenna were simulated by placing them face-to-face in free space with 50 mm separation between them. One antenna acts as transmitter and the second antenna as receiver. Two time domain signals, the source signal $s(t)$ delivered to the transmitter terminal, and the signal $r(t)$ received by the receiver, are used to calculate fidelity. The time derivative of the source signal is then normalized to its energy to give $\hat{s}(t)$, while the received signal is normalized to its energy to give $\hat{r}(t)$. Antenna fidelity, $F$, is the maximum magnitude of the cross correlation between $\hat{s}(t)$ and $\hat{r}(t)$ and is calculated using (5) as shown below [19]

$$F = \max_{\tau} \int_{-\infty}^{\infty} \hat{r}(t - \tau)\,\hat{s}(t)\,dt \tag{5}$$

For $F = 1$, the two signals are identical, and for $F = 0$, the two signals are entirely different from each other. This method of fidelity evaluation includes the signal distortion produced by both transmitter and receiver antennas.

In our analysis, the fidelity in the case of 50 mm of free space between the two antennas is found to be 0.9718, which represents good matching between the transmitted and received signals. To investigate the effect of the breast on the antenna signal distortion, two phantoms have been used. Each phantom has a 50 mm thickness in order to compare it with the results of 50 mm of free space. Thus, the first phantom consists of two layers of skin, each layer is 1.5 mm, and a 47 mm thick layer of fat-median between them. The second phantom has five layers arranged symmetrically between the two antennas. The configuration of these layers are: 1) a skin 1.5 mm. 2) fat-median 17 mm. 3) a 13 mm of glandular-low. 4) fat-median of 17 mm and, 5) a 1.5 mm skin.

For simulation, the frequency dependent skin permittivity and conductivity values were obtained from databases [20]. The dispersion curves of fat and glandular were calculated according to Eqs. (6), (7), and (8) below [21, 22]. For better accuracy, a 2nd order fitting curve is used in the calculation.

$$\varepsilon_r(\omega) = \varepsilon_\infty + \frac{\Delta\varepsilon}{1 + (j\omega\tau)^{1-\alpha}} + \frac{\sigma_s}{j\omega\varepsilon_o} \tag{6}$$

$$\varepsilon_r'(\omega) = \varepsilon_\infty + \left[1 - \frac{\sinh(\beta\ln(\omega\tau))}{\cosh(\beta\ln(\omega\tau)) + \cos\left(\frac{\beta\pi}{2}\right)}\right] * \frac{\Delta\varepsilon}{2} \tag{7}$$

$$\varepsilon_r''(\omega) = \frac{\sin\left(\frac{\beta\pi}{2}\right)}{\cosh(\beta\ln(\omega\tau)) + \cos\left(\frac{\beta\pi}{2}\right)} * \frac{\Delta\varepsilon}{2} + \frac{\sigma_s}{\omega\varepsilon_o} \tag{8}$$

Here $\varepsilon_r$ is the complex relative permittivity, and $\varepsilon_r'$ and $\varepsilon_r''$ represent the real and imaginary parts of the dielectric constant, respectively. $\varepsilon_\infty$ = relative permittivity at infinite frequency, $\Delta\varepsilon = \varepsilon_s - \varepsilon_\infty$, where $\varepsilon_s$ is the relative permittivity related to the relaxation process; $\sigma_s$ is the static ionic conductivity; $\tau$ and $\tau_o$ are the time constants; $\alpha$ and $\beta$ are the degree of relaxation distribution. The dispersion curves of the skin, fat-median, and glandular-low layers are plotted in Fig. 7.

The antenna fidelities corresponding to the first and second phantoms are 0.8094, and 0.5423, respectively. Compared to free space value, the fidelities of the first phantom and second phantom deterioration are mainly because of the layers of the breast phantom and thus increasing signal reflections and attenuations. The frequency dependent permittivity value of the glandular layer, which is high compared to the fat layer, adds complication of the layers.
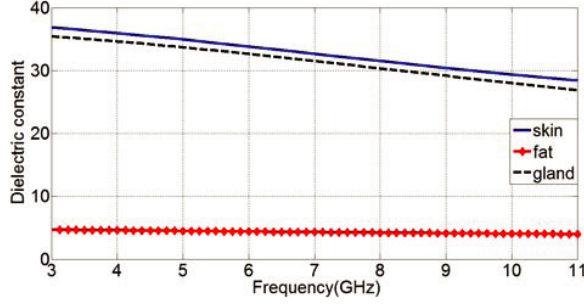
**Figure 7.** Dielectric constant versus frequency of breast phantom tissues.
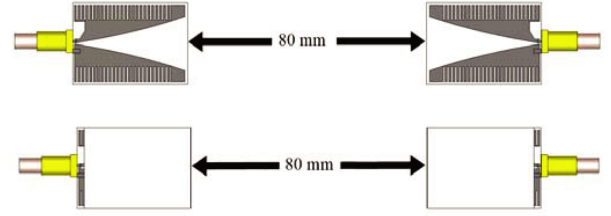


**Figure 8.** Antennas setup to measure group delay. (top) Without dielectric layers. (bottom) with dielectric.
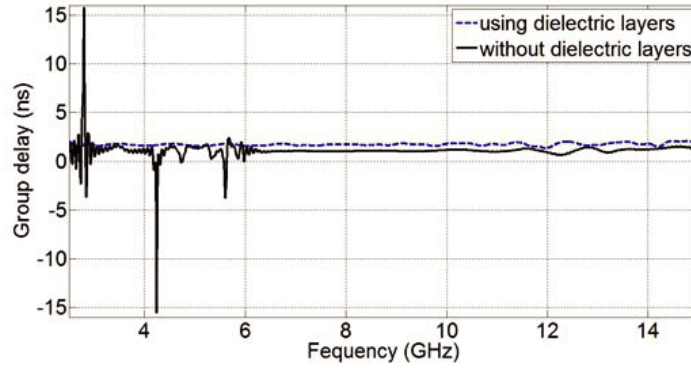


**Figure 9.** Group delay of the antenna.

To investigate this effect of the dielectric layers on signal distortion, the antenna time domain response was tested with and without embedding the antenna in the dielectric layers. Distortion of signals is usually measured by the group delay which should be nearly constant to ensure low distortion. Two antennas were positioned face-to-face in free space with a distance of 80 mm between them as shown in Fig. 8. The transmitted signal is an UWB Gaussian signal. The group delay for the whole band of the antenna was evaluated and plotted in Fig. 9. As shown in Fig. 9, without covering the antenna with dielectric layers, the antenna group delay has many high peaks, especially at frequencies less than 7 GHz. After embedding the antenna in dielectric layers, antenna group delay becomes smooth and more stationary. The group delay in the band used for medical applications (3.1 GHz to 10.6 GHz) becomes almost constant with peak to peak fluctuation of only 0.3 ns. This suggests that the proposed antenna successfully meets the time domain test. Coupled with previous results it can be stated that the designed antenna can be a strong candidate for breast cancer detection.

## 4. $S$-PARAMETERS ANALYSIS WITH BREAST TUMOR

Our imaging setup is similar to that presented by Amineh et al [15], but with modifications, as discussed later. The imaging setup in [15] uses two antennas, one to send a UWB signal and the other to receive it, to accomplish a 2-D scan in the $yz$ plane. The breast is compressed between the antennas, and the antennas move together in fixed steps until the breast is completely scanned. The duration of the signal is in the nanosecond regime at a given breast location and therefore the heating effect can be neglected. The image was formed as follow: — First the phantom without tumors was placed between the antennas and the transmission $S$-parameter between the two antennas at each position $(yz)$ was recorded as $S_{21}^{back}(yz)$. Then the same phantom with many tumors was placed between the two antennas to get the measured transmission $S$-parameter $S_{21}^{meas}(yz)$. The image was acquired by subtracting transmission $S$-parameter of phantom with no tumors from transmission $S$-parameter of

phantom with tumors at each position then taking the absolute value as in (9) [15].

$$\left| S_{21}^{image} \right| = \left| S_{21}^{meas}(y,z) - S_{21}^{back}(y,z) \right| \tag{9}$$

Unfortunately, when a breast is tested for cancer in clinics, there are no background data that can be subtracted from the measured transmission $S$-parameter. Thus, an alternative solution is required to obtain images without background data.

To detect tumors without the need of background information, we simulated two of our proposed antennas and placed them face-to-face with 40 mm separation between them. One antenna transmits a signal, and the other receives it. Both the transmission $S$-parameter ($S_{21}$) and reflection $S$-parameter ($S_{11}$) are saved at all frequencies from 3.1 GHz to 10.6 GHz. After that, a spherical shape tumor placed in mid-distance between the two antennas is simulated, as shown in Fig. 10(a). The radius of the spherical tumor is 6 mm, and the relative dielectric constant versus frequency is calculated from Eq. (7) and shown in Fig. 10(b). $S_{21}$ and $S_{11}$ are then recorded with the tumor. The purpose of this test is to study the effect of tumor on $S_{21}$ and $S_{11}$ at the frequency band of interest and then find a clue in the $S$-parameters to form breast images without the need of background data. We explain as follows. Figs. 10(c) and 10(d) show the effect of tumor on $S_{11}$ and $S_{21}$ parameters, respectively. At low frequencies in (Fig. 10(c)), there is an increase of reflection coefficient when the tumor is present as compared to an absence of tumor. On the other hand, at increasing frequencies the tumor impedes the transmission of the incoming signal, as shown in Fig. 10(d). Thus, at frequencies below 7 GHz we might expect scattering of signals by the tumor, while it absorbs the signal above 7 GHz. Exploiting the difference in $S_{11}$ at low frequencies and $S_{21}$ differences at high frequencies is the key to eliminate the requirement of background information.
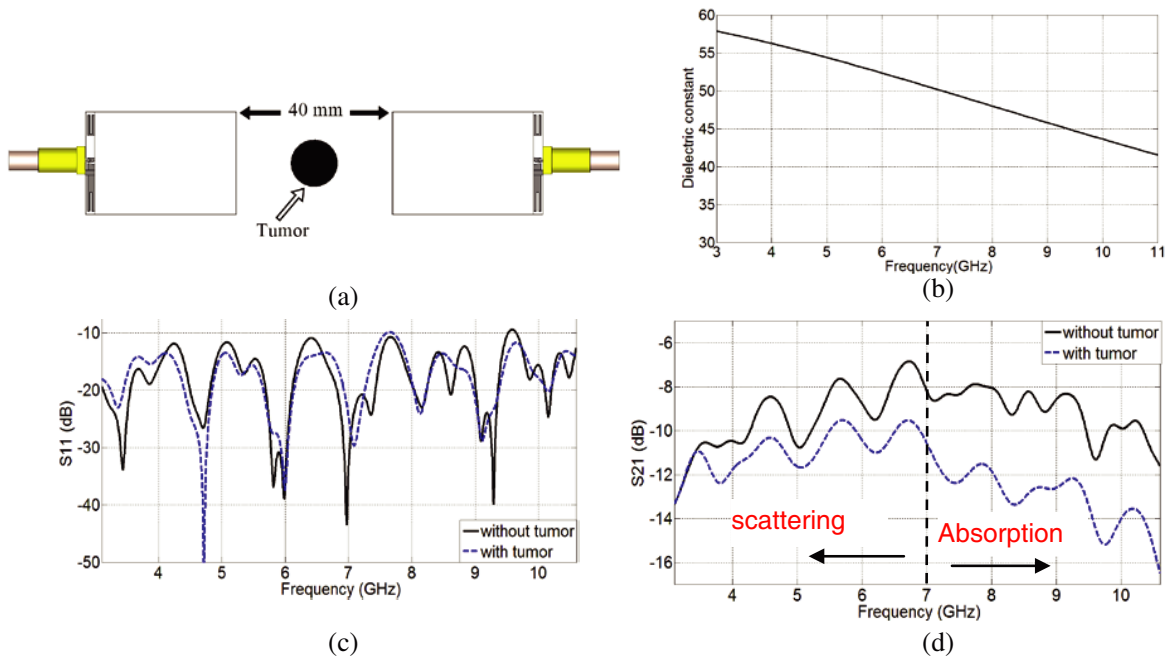


**Figure 10.** Measuring $S$-parameters. (a) Measurement setup. (b) Dielectric constant versus frequency of malignant tumor. (c) $S_{11}$. (d) $S_{21}$.

## 5. IMAGING SETUP AND ACQUISITION APPROACHES

The previous section shows the frequency dependent reflection and transmission parameters changes due to the presence of tumors. We exploit this effect in tumor detection, and then use [15] for image construction setup. The breast to be tested is slightly compressed between the transmitting and receiving antennas. The purpose of breast compressing is to make the breast surface as flat as possible for 2D scanning.

The change in $S$-parameters in Figs. 10(c) and 10(d) is reduced when a tumor is present in the breast phantom instead of free space. This is due to multi-layer reflections. The reduction in $S_{11}$ will be more than that of $S_{21}$ because multi-layers reduce the detected reflection from the tumor. Also, the difference in $S_{11}$, shown in Fig. 10(c), is less than the difference of $S_{21}$ in Fig. 10(d). Based on these observations, we present two approaches to form images for tumor detection.

The first approach is based on $S_{21}$ variation with and without tumor present at high frequency. Consider the case in Fig. 11(a) where the breast area $A_{breast}$ in the $yz$ plane bounded by $y1$, $z1$ to $y2$, $z2$ is to be scanned. Inside $A_{breast}$ there is a tumor located at distance $x$, and its area in the $yz$ plane is $A_{tumor}$. The transmission $S_{21}$ parameter between the two antenna is minimum when the antennas are at the $yz$ point corresponding to $A_{tumor}$. In contrast, the transmission $S_{21}$ parameter increases when the antennas are at any $yz$ point in $A_{breast}$ outside of $A_{tumor}$. Thus, subtracting the maximum $S_{21}$ value from all other $S_{21}$ values in $A_{breast}$ and taking its absolute value can identify the tumor location. Squaring the absolute value increases the contrast between the subtracted values. However, the difference in the $S_{21}$ parameter at the tumor position and at a point far from the tumor is not large, specifically when the breast phantom has layers, such as skin and fat. The variation in $S_{21}$ can be increased by squaring the subtraction results. Our equation to form an image of $A_{breast}$ is:

$$I_{yz} = k1 * \left| (S_{21})_{yz} - (S_{21})_{max} \right|^2 \tag{10}$$

where $I_{yz}$ is an element in the image matrix corresponding to the $yz$ position. $k1$ is just a scaling factor in this approach, $(S_{21})_{yz}$ the $S_{21}$ parameter when the antennas are at the $yz$ position, and $(S_{21})_{max}$ the highest value of $(S_{21})_{yz}$.

The image matrix covers all $A_{breast}$ and has a size that depends on the antennas' scanning step size in the $yz$ plane.

Eq. (10) can be applied to find the tumor image on the high frequency side of the band (3.1 GHz to 10.6 GHz), for example, 9 GHz.

The second tumor imaging approach is based on the variations in $S_{11}$ and the reflection increment at a tumor position. This approach is as the previous approach with the following differences: (i) The second approach uses the $S_{11}$ parameter instead of the $S_{21}$ parameter. (ii) The minimum value of $S_{11}$ is subtracted from all values of the $S_{11}$ parameter because the reflection is maximum at tumor position. (iii) The $S_{11}$ parameter is taken from the low frequency side of the 3.1 GHz to 10.6 GHz frequency band. (iv) As mentioned earlier, the variation in $S_{11}$ in Fig. 10(c) is less than the variation in $S_{21}$ in Fig. 10(d), so the power of the image element equation should be increased from 2 to higher value to obtain enough contrast, the value of 8 gives enough contrast and is therefore used in our calculations. The image matrix element, $I_{yz}$ at $yz$ position can be obtained as:

$$I_{yz} = k2 * \left| (S_{11})_{yz} - (S_{11})_{min} \right|^8 \tag{11}$$

where $k2$ is a scaling factor in the second approach, and $(S_{11})_{min}$ is the lowest value of $(S_{21})_{yz}$. To obtain a better image display, the image matrix can be modified to a bigger size by using Matlab which interpolates the image matrix elements. The scaling factors used here are $k1 = 10$ and $k2 = 5$. For all imaging tests, the scanning step size used is 5 mm in both the horizontal and vertical antennas movement.

Many breast phantoms were simulated in evaluating the antenna and imaging. The first phantom was 43 mm thick with two 1.5 mm skin layers and a 40 mm fat layer between them. The breast phantom was placed between the two identical antennas. The scanned area was 60 mm by 75 mm in the $y$ and $z$ directions, respectively. Two tumors were placed in the phantoms at 20 mm under the skin layer as shown in Figs. 11(a) and 11(b). The first tumor was elliptical in shape, with a center at $y = 21$ mm, $z = 20$ mm, and radii 5 mm and 7.5 mm. The second tumor was a sphere, 4 mm in radius and centered at $y = 45$ mm, $z = 41$ mm.

$S_{21}$ parameter was evaluated at all positions using 9 GHz in the first technique. This frequency was chosen as the high value in the frequency band. On the other hand, low frequency is required in the second technique, 4 GHz is selected. The images formed using the first approach and second approach are shown in Figs. 11(c), and 11(d), respectively. The white ellipse and circle represent the real shapes, locations and size of the tumors. From the images in Fig. 11, we conclude the following:
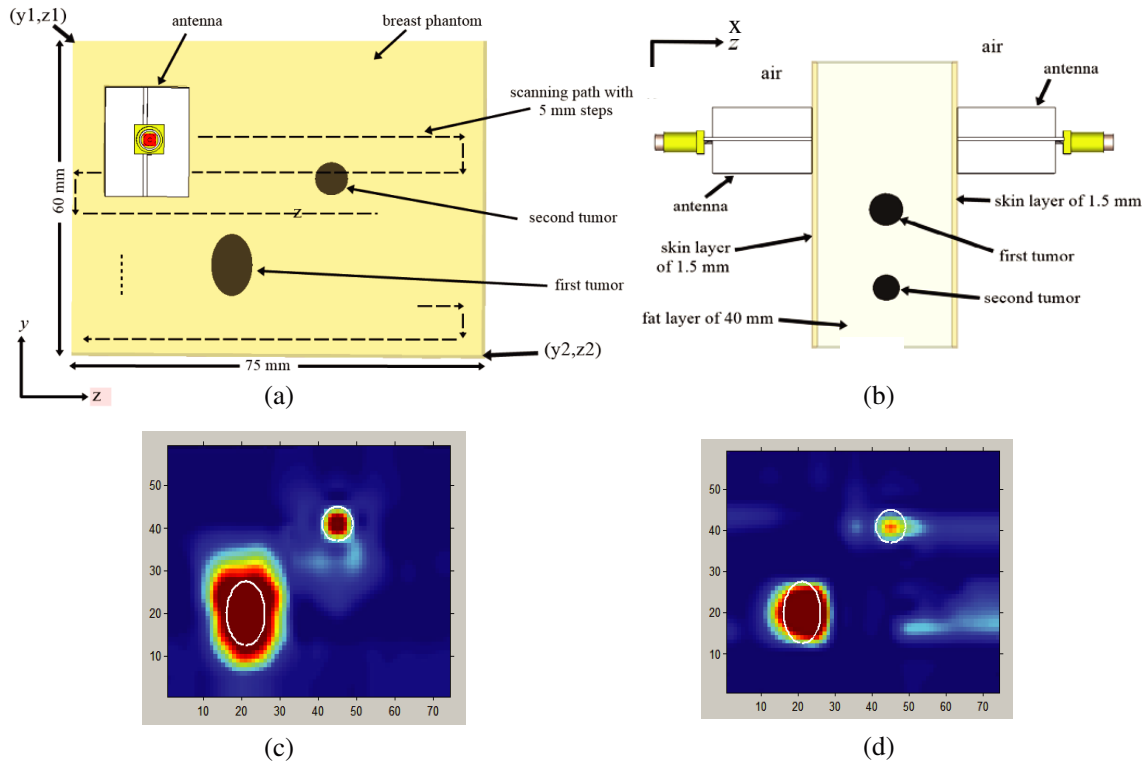
**Figure 11.** (a) Microwave imaging setup of breast phantom with two tumors (Side view). (b) Microwave imaging setup of breast phantom with two tumors (Top view). (c) Formed image using first approach at 9 GHz. (d) Formed image using second approach at 4 GHz.

(i) Both approaches can detect the tumors without background data. (ii) The actual locations of the tumors are correctly identified in both techniques. (iii) The first technique determines the real size of the circular small tumor, and enlarges the size of the elliptical big tumor as shown in Fig. 11(c). This is because the first approach depends on the transmission $S$-parameter; and the big tumor reduces the transmission between the two antennas even when the tumor is not exactly at the center point of the antenna. (iv) For the second approach in Fig. 11(d), the size of the big tumor is nearly correct, however the size of the small tumor shrinks. The shrinking is caused in the second technique since it depends on the reflection $S$-parameter.

We have stated earlier that the first imaging approach is valid for high frequencies in the 3.1 GHz to 10.6 GHz band, while the second is for low frequencies in the band. In order to prove this hypothesis, the two approaches are applied for breast imaging at incorrect frequencies. The same phantom and imaging setup shown in Fig. 11 is used in this test. For the first technique using $S_{21}$, the test is conducted at 4 GHz and at 7 GHz instead of 9 GHz. The obtained images are shown in Figs. 12(a),(b) for 4 GHz and 7 GHz, respectively. At 4 GHz, only the big tumor is detected and its shape is different than the original one. When the frequency increases to 7 GHz, the image for the big tumor improves while the small tumor starts to appear blurred.

For the second approach using $S_{11}$, the images are formed at 6.5 GHz and 9 GHz frequencies instead of 4 GHz. The resulting images are shown in Figs. 12(c) and (d) for 6.5 GHz and 9 GHz, respectively. As expected, at both frequencies, the tumor detection fails. This is because the reflected signal attenuation increases as the frequency increases and this technique is based on reflection intensity of the tumor. Even the big tumor does not appear in the test images. The detection with the second approach totally fails at 6.5 GHz and 9 GHz, while the first approach can detect the big tumor at 4 GHz and 7 GHz. Consider Figs. 10(c) and 10(d), where Fig. 10(d) shows the difference in the $S_{21}$ from 3.1 GHz to 10.6 GHz with and without the presence of tumor. The difference increases with increasing frequency, and at 9 GHz the simulation shows maximum difference over the rest simulated frequencies in the first

(a)  (b)  (c)  (d)
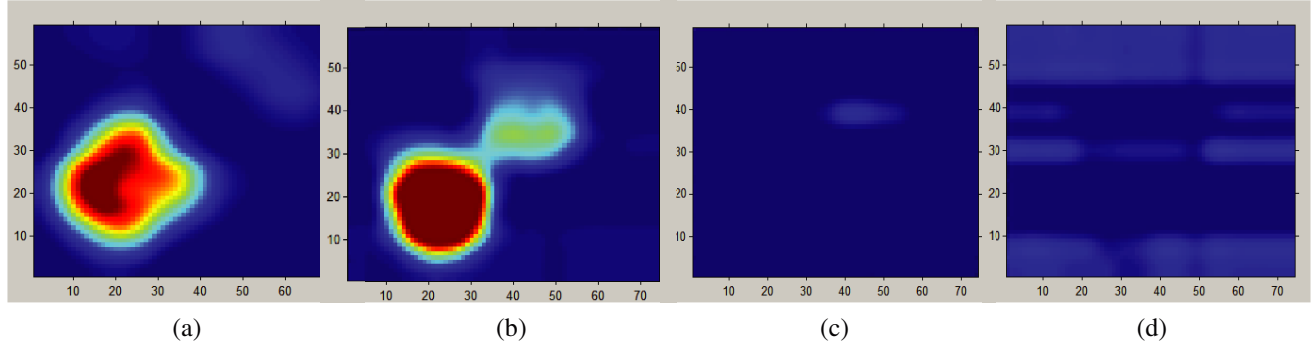
**Figure 12.** Formed images. (a) First approach at 4 GHz. (b) First approach at 7 GHz. (c) Second approach at 6.5 GHz. (d) Second approach at 9 GHz.



(a)  (b)



(c)  (d)
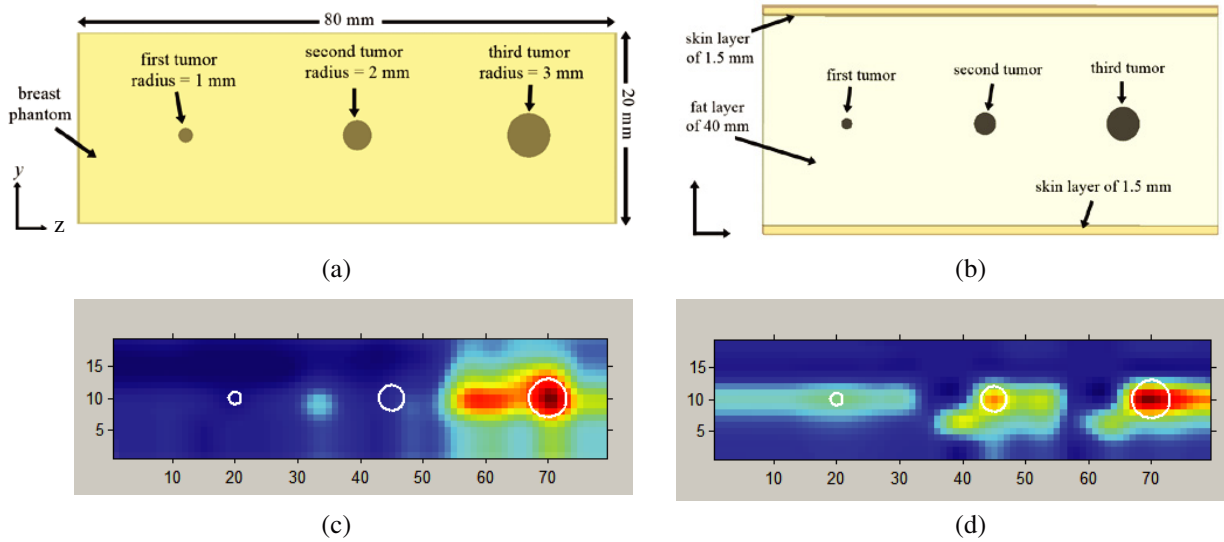
**Figure 13.** (a) Breast phantom with three small tumors. (Side view). (b) Breast phantom with three small tumors. (Top view). (c) Formed image using first approach 3-tumor case at 9 GHz. (d) Formed image using second approach 3-tumor case at 4 GHz.

approach. However, the second approach has a limited frequency band on the low side of the 3.1 GHz to 10.6 GHz band. This limited band, where $S_{11}$ with tumor significantly exceeds $S_{11}$ with no tumor, starts from 3.1 GHz and goes to almost 4.2 GHz, as shown in Fig. 10(c). Therefore, we conclude that the second technique is valid for very lower frequencies of the assigned frequency band, and the first technique is applicable to the higher frequencies of that band.

To test the capability of the antenna and our imaging approaches for detecting small tumors, a breast phantom with different embedded tumor sizes was simulated. The breast parameters are the same as in the phantom used in Fig. 11 but in this case the tumors, as well as the scanned area, are different. The scanned aperture is a rectangle 20 mm and 80 mm in the $y$ and $z$ directions, respectively. Three spherical tumors are simulated inside the phantom, 20 mm under the skin layer and at $y = 10$ mm as shown in Figs. 13(a) and 13(b). Moving from left to right, the first tumor is of 1 mm radius, the second tumor is of 2 mm radius, and the third tumor is of 3 mm radius located at $z = 20$ mm, 45 mm, and 70 mm, respectively.

An aperture 2D raster scan is applied, and the acquired images are shown in Figs. 13(c) and 13(d) for the first and second approaches, respectively. The first approach using $S_{21}$ is at 9 GHz, whereas 4 GHz is chosen for the second approach using $S_{11}$. Only the largest tumor of 3 mm radius is detected by the first approach (Fig. 13(c)). On other hand, the second approach detects the largest tumor and

the medium tumor. In addition, the smallest tumor of 1 mm radius appears as a ghost using the second technique. The scanning step size is 5 mm which is much larger than the small tumor of 1 mm radius. If the scanning step size is reduced, the smallest tumor may be detected as well.

The human breast has many layers, such as skin, fat, and glands. When the number of layers increases, the reflections of the microwave signals inside the breast also increase which complicates the tumor detection process. In order to test our antenna and image acquisition approaches for this case, a breast phantom having skin, fat and gland layers was simulated. This full breast phantom consists of five layers organized symmetrically between the two antennas. The phantom layers are: i) a skin, 1.5 mm thickness, ii) a 10 mm fat-median layer, iii) a 10 mm of glandular-low iv) fat-median layer of 10 mm and, v) a 1.5 mm skin layer. An elliptical tumor was placed in the middle of the glandular layer. The radii of the tumor are 4 mm and 3 mm and its center is at $y = 10$ mm, $z = 15$ mm. The dispersion curves for the skin, fat-median, glandular-low layers and the tumor are obtained by Equation (7) and plotted in Figs. 7 and 10(b). The scanned breast area is 20 mm in $y$-direction by 40 mm in $z$-direction.

The obtained images from the full breast phantom with step size of 5 mm are shown in Figs. 14(a) and 14(b) for the first and second approaches, respectively. Both the approaches are capable of detecting the tumor in the multi-layer breast scenario. However, the second approach detects the tumor with the color red (indicating high intensity) and it shows a smearing on the sides of the tumor with lighter color (indicating lower intensity). The cause for the smearing is the reflections in the interface between fat and glandular layers near the tumor.

To solve the smearing problem in the second approach, the difference in $S_{11}$ between the tumor absent case and tumor present case needs to be emphasized in the full breast phantom case. Increasing the contrast in the images is achieved by increasing the power in Equation (11) from 8 to a higher number. Fig. 14(c) shows the acquired image of the full phantom using the second approach after increasing the power in Equation (11) from 8 to 50. In Fig. 14(c) the smearing is minimized and the tumor shape is optimally fixed in the white ellipse which represents the actual shape and position of the tumor.



|  (a)  |  (b)  |  (c)  |
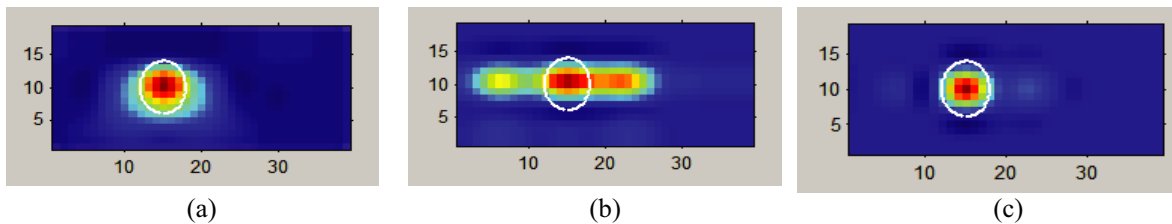
**Figure 14.** Formed images. (a) First approach at 9 GHz. (b) Second approach at 4 GHz and (c) formed images after modification of the second approach.

## 6. CONCLUSIONS

An ultra-wideband, modified tapered slot antenna has been designed for breast imaging and cancer detection in the microwave range. Compactness and high directivity for the antenna is achieved without the necessity of coupling liquid which increases losses and complicates the imaging system setup and maintenance. At each location of the breast, the antenna transmits a very short Gaussian pulse then moves to another location, so the skin heating effect can be neglected. Covering the antenna by two layers of dielectric material has improved impedance matching, increased directivity, and reduced time domain signal distortion. The antenna performance in breast cancer detection was tested by applying raster scan imaging on several breast phantoms. Two approaches were presented to detect tumors without the need of breast background information. The approaches exploit the effect of tumor on $S_{11}$ and $S_{21}$ at specific frequency bands. The antenna was used to detect tumors in different breast phantom structures including multi-layer composite phantom. The antenna test results demonstrate attractive performance. In addition, the obtained images prove the capability of the antenna in tumor detection even for small tumors and multi-layer phantom cases.

## REFERENCES

1. Allen, B., M. Dohler, E. E. Okon, W. Q. Malik, A. K. Brown, and D. J. Edwards, *Ultra Wideband Antennas and Propagation for Communications, Radar and Imaging*, John Wiley & Sons Ltd, Chichester, England, 2007.

2. Fear, E. C., S. C. Hagness, P. M. Meaney, M. Okoniewski, and M. A. Stuchly, "Enhancing breast tumor detection with near-field imaging," *IEEE Microwave Magazine*, Vol. 3, No. 1, 48–56, March 2002.

3. Sarafianou, M., I. J. Craddock, and T. Henriksson, "Towards enhancing skin reflection removal and image focusing using a 3-D breast surface reconstruction algorithm," *IEEE Transactions on Antennas and Propagation*, Vol. 61, No. 10, 5343–5346, June 2013.

4. Li, X., S. K. Davis, S. C. Hagness, D. W. van der Weide, and B. D. Van Veen, "Microwave imaging via space-time beamforming: Experimental investigation of tumor detection in multilayer breast phantoms," *IEEE Transactions on Microwave Theory and Techniques*, Vol. 52, No. 8, 1856–1865, August 2004.

5. Abbosh, A. M., "Miniaturized microstrip-fed tapered-slot antenna with ultrawideband performance," *IEEE Antennas and Wireless Propagation Letters*, Vol. 8. 690–692, June 2009.

6. Waterhouse, R., *Printed Antennas for Wireless Communications*, Chapter 6: Printed Tapered Slot Antennas, John Wiley & Sons, Chichester, England, 2007.

7. Xu, H.-Y., H. Zhang, J. Wang, and L.-X. Ma, "A new tapered slot antenna with symmetrical and stable radiation pattern," *Progress In Electromagnetics Research Letters*, Vol. 5, 35–43, 2008.

8. Adamiuk, G., T. Zwick, and W. Wiesbeck, "Compact, Dual-polarized UWB-antenna, embedded in a dielectric," *IEEE Transactions on Antennas and Propagation*, Vol. 58, No. 2, 279–286, February 2010.

9. Bourqui, J., M. Okoniewski, and E. C. Fear, "Balanced antipodal vivaldi antenna with dielectric director for near-field microwave imaging," *IEEE Transactions on Antennas and Propagation*, Vol. 58, No. 7, 2318–2326, July 2010

10. Mohammed, B. J., A. M. Abbosh, D. Ireland, and M. E. Bialkowski, "Compact wideband antenna for microwave imaging of brain," *Progress In Electromagnetics Research C*, Vol. 27, 27–39, 2012.

11. Teni, G., N. Zhang, J. Qiu, and P. Zhang, "Research on a novel miniaturized antipodal Vivaldi antenna with improved radiation," *IEEE Antennas and Wireless Propagation Letters*, Vol. 12, 417–420, March 2013.

12. Chen, L., Z. Lei, R. Yang, J. Fan, and X. Shi, "A broadband artificial material for gain enhancement of antipodal tapered slot antenna," *IEEE Transactions on Antennas and Propagation*, Vol. 63, No. 1, 395–400, October 2014.

13. Pandey, G. K., H. S. Singh, P. K. Bharti, A. Pandey, and M. K. Meshram, "High gain Vivaldi antenna for radar and microwave imaging applications," *Transactions on International Journal of Signal Processing Systems*, Vol. 3, No. 1, 35–39, June 2015.

14. Larsen, L. E. and J. H. Jacobi, *Medical Applications of Microwave Imaging*, IEEE Press, New York, 1985.

15. Amineh, R. K., M. Ravan, A. Trehan, and N. K. Nikolova, "Near-field microwave imaging based on aperture raster scanning With TEM horn antennas," *IEEE Transactions on Antennas and Propagation*, Vol. 59, No. 3, 928–940, March 2011.

16. Khalatpour, A., R. K. Amineh, H. Xu, Y. Baskharoun, and N. K. Nikolova, "Image quality enhancement in the microwave raster scanning method," *2011 IEEE MTT-S International Microwave Symposium*, 1–4, Baltimore, MD, 2011.

17. Fei, P., Y.-C. Jiao, Y. Ding, and F.-S. Zhang, "A compact coplanar waveguide fed wide tapered slot ultra-wideband antenna," *Progress In Electromagnetics Research Letters*, Vol. 25, 77–85, 2011.

18. Zhu, F., S. Gao, A. TS Ho, and T. Brown, "Compact size asymmetric linearly tapered slot antenna for portable ultra-wideband imaging radar system," *Radar Systems IET International Conference*, 1–4, Glasgow, UK, 2012.

19. Li, X., S. C. Hagness, M. K. Choi, and D. W. van der Weide, "Numerical and experimental investigation of an ultrawideband ridged pyramidal horn antenna with curved launching plane for pulse radiation," *IEEE Antennas and Wireless Propagation Letters*, Vol. 2, No. 1, 259–262, 2003.

20. Gabriel, S., R. W. Lau, and C. Gabriel, "The dielectric properties of biological tissues: III. Parametric models for the dielectric spectrum of tissues," *Phys. Med. Biol.*, Vol. 41, 2271–2293, 1996.

21. Zastrow, E., S. K. Davis, M. Lazebnik, F. Kelcz, B. D. V. Veen, and S. C. Hagness, "Development of anatomically realistic numerical breast phantoms with accurate dielectric properties for modeling microwave interactions with the human breast," *IEEE Transactions on Biomedical Engineering*, Vol. 55, No. 12, 2792–2800, December 2008.

22. Maher, A. and K. M. Quboa, "Development of accurate UWB dielectric properties dispersion at CST simulation tool for modeling microwave interactions with numerical breast phantoms," *Eighth International Multi-Conference on Systems, Signals & Devices (SSD 11)*, Sousse, Tunisia, 2011.